

Six-Degree-of-Freedom Localization With a 3-Axis Accelerometer and a 2-Axis Magnetometer for Magnetic Capsule Endoscopy

Adam J. Sperry¹, Student Member, IEEE, Jordan J. Christensen¹, and Jake J. Abbott¹, Senior Member, IEEE

Abstract—This letter presents a new localization method for magnetic capsule endoscopes that uses sensors internal to the capsule, but aims to relieve some of the previous limitations associated with this paradigm. The method estimates the six-degree-of-freedom capsule pose with no prior pose information other than the knowledge that it resides within a particular workspace. Internal to the capsule, it requires a 3-axis accelerometer, a 2-axis magnetometer (or 3-axis magnetometer with one axis saturated or disabled), a microcontroller capable of wireless communication, and a radio frequency antenna, all of which can be integrated into a single printed circuit board. The method is applicable to both of the common configurations of the internal permanent magnet. In a set of simulations and experiments, we show that the localization accuracy is comparable to what has been obtained with prior methods that have required more complexity.

Index Terms—Medical robots and systems, localization.

I. INTRODUCTION

WIRELESS capsule endoscopes are increasingly employed for non-invasive inspection of the gastrointestinal tract. Localization and control of such capsules is an active area of recent research, with the goal of improving their clinical effectiveness [1]. The use of magnetic fields for both localization and control of these capsules has been established as a feasible approach due to their negligible attenuation through biological tissues at low frequencies and their ability to apply contactless force and torque.

Two main paradigms exist for magnetic-field-based localization of capsule endoscopes, both of which rely on a magnetic source and a set of sensors capable of measuring that source [2]. The two paradigms are characterized by the source being external/internal to the capsule and the sensors being internal/external to the capsule. Current methods that place the sensors external to the capsule reduce power and space constraints on the capsule design; however, they have workspace limitations, estimate less than the full 6-degree-of-freedom (6-DOF) pose, and require

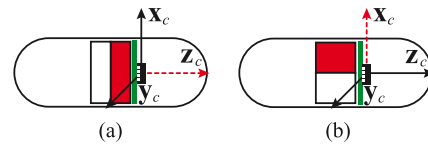


Fig. 1. The two most common magnetization directions used in magnetic capsule endoscopes, in which the dipole is either (a) aligned with or (b) orthogonal to the capsule's major axis. The red dashed axis indicates the saturated, and thus unusable, magnetic sensing direction of the magnetometer.

large sensor arrays that must be calibrated [3]–[9]. Current solutions employing internal sensors address these issues, but they consume more of the limited on-board space and power, and they need complicated sensor arrangements [10]–[13].

This letter presents a new localization method that uses sensors internal to the capsule, but aims to relieve some of the previous limitations associated with this paradigm. The method estimates the 6-DOF capsule pose with no prior pose information other than the knowledge that it resides within a particular workspace. Internal to the capsule, it requires a 3-axis accelerometer, a 2-axis magnetometer (or 3-axis magnetometer with one axis saturated or disabled), a microcontroller capable of wireless communication, and a radio frequency antenna. All of these components can be purchased commercial off-the-shelf (COTS), potentially as an integrated inertial measurement unit (IMU), and placed on a single circular printed circuit board (~3–4 mm thick, including components) in close proximity to the internal magnet used for actuation. The magnetization direction of the internal magnet in most capsule designs is either along the capsule's major axis (e.g., when controlling the camera axis [13], [14]) or orthogonal to the major axis (e.g., in screw-type capsules [11], [15], [16]). This results in one axis of the magnetometer being saturated by the internal magnet, rendering it unusable (Fig. 1). It is also common for one sensing axis of a COTS 3-axis magnetometer to have a different resolution from the other two (typically the z-axis in Fig. 1). As such, we characterize our localization method for the two cases of the two magnetic sensing directions having the same or different resolution.

Finally, in [12], a continuously rotating external magnetic dipole field is used to perform the localization. This approach requires synchronization of the clocks of the capsule microcontroller and the host computer to time-register external dipole orientations with corresponding magnetometer measurements.

Manuscript received September 8, 2021; accepted January 5, 2022. Date of publication January 14, 2022; date of current version January 25, 2022. This letter was recommended for publication by Associate Editor K. Rabenorosoa and Editor J. Burgner-Kahrs upon evaluation of the reviewers' comments. This work was supported by the National Science Foundation under Grant 1830958. (Corresponding author: Adam J. Sperry.)

The authors are with the Department of Mechanical Engineering and the Robotics Center, University of Utah, Salt Lake City, UT 84112 USA (e-mail: adam.sperry@utah.edu; jordan.christensen@utah.edu; jake.abbott@utah.edu). Digital Object Identifier 10.1109/LRA.2022.3143293

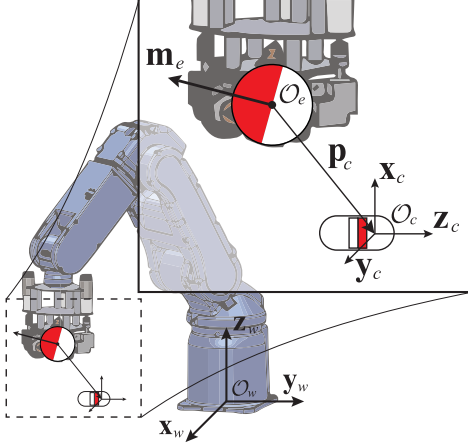


Fig. 2. Depiction of the reference frames involved in the localization method. The (arbitrary) world frame at \mathcal{O}_w is fixed. \mathcal{O}_e is the position of the center of the external magnetic dipole with moment \mathbf{m}_e , which is known. The frame at \mathcal{O}_c is the sensing frame of the magnetometer and defines the pose of the capsule, where \mathbf{p}_c is the relative position vector from \mathcal{O}_e to \mathcal{O}_c .

In this letter, we investigate the use of a fixed set of external dipole orientations, which relaxes the need for precise clock synchronization.

II. LOCALIZATION METHOD

We assume a sensor package, internal to the capsule, comprising a 3-axis accelerometer and a magnetometer measuring the magnetic field along two cardinal axes of a reference frame, with origin \mathcal{O}_c , fixed within the sensor (see Fig. 2). The sensor package is placed in close proximity to the internal permanent magnet that is used for magnetic actuation such that the two active magnetic sensing directions are minimally affected by the strong dipole field. Also assume an external magnetic dipole with fixed magnitude and known center position \mathcal{O}_e . The external dipole could be a permanent magnet positioned by a robotic manipulator (as in Fig. 2), or an electromagnetic dipole source (e.g., [17]). During localization, the position of the external dipole is kept fixed, but the direction of the dipole moment \mathbf{m}_e (units $\text{A} \cdot \text{m}^2$) is allowed to change. We assume that the capsule remains stationary during localization, which assumes that the external dipole is sufficiently weak or far from the capsule.

The goal of localization is to estimate the 3-DOF position, $\mathbf{p}_c = \mathcal{O}_c - \mathcal{O}_e$ (units m), and 3-DOF orientation, \mathbf{R}_c , of the magnetometer frame, which is taken to be the pose of the capsule. Note that, with \mathbf{p}_c determined, the capsule position relative to the world frame origin \mathcal{O}_w can be computed using knowledge of \mathcal{O}_e . \mathbf{R}_c is the 3×3 rotation matrix that rotates the capsule frame to align with the fixed world reference frame and can be decomposed using ZYX Euler angles into

$$\mathbf{R}_c = \mathbf{R}_z(\psi)\mathbf{R}_y(\theta)\mathbf{R}_x(\phi) \quad (1)$$

where ψ , θ , and ϕ are the Z, Y, and X Euler angles, respectively. The θ and ϕ angles can be estimated directly from the accelerometer reading, $\mathbf{g} = [g_x \ g_y \ g_z]^T$, by

$$\theta = \text{atan2}\left(-g_x, \sqrt{g_y^2 + g_z^2}\right) \quad (2)$$

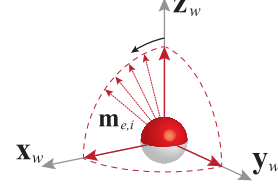


Fig. 3. Moments used when collecting magnetometer measurements $\mathbf{m}_{e,i}$. The moments are evenly spaced tracing out the three arcs of an octant.

$$\phi = \text{atan2}(g_y, g_z). \quad (3)$$

Note that we restrict ψ and ϕ to the interval $[-\pi, \pi]$ rad and θ to the interval $[-\pi/2, \pi/2]$ rad. Using atan2 in (2) satisfies this constraint because the second argument is always non-negative. With θ and ϕ known, \mathbf{p}_c and ψ are left to be estimated with the magnetometer.

We assume that the field \mathbf{b} (units T) from the external dipole, as measured by the magnetometer, can be accurately modeled using the point-dipole equation [18]:

$$\mathbf{b} = \mathcal{B} \left[\left(\frac{3\mathbf{p}_c\mathbf{p}_c^T}{\|\mathbf{p}_c\|^2} - \mathbf{I} \right) \frac{\mathbf{m}_e}{\|\mathbf{m}_e\|} \right], \quad \mathcal{B} = \frac{\mu_0\|\mathbf{m}_e\|}{4\pi\|\mathbf{p}_c\|^3} \quad (4)$$

where \mathcal{B} (units T) is the nominal field strength at a given distance from the dipole moment, the term in square brackets encodes the dimensionless direction with respect to the dipole moment, $\mu_0 = 4\pi \times 10^{-7} \text{ T} \cdot \text{m/A}$ is the permeability of free space, and \mathbf{I} is the identity matrix. At a given distance $\|\mathbf{p}_c\|$, the field strength can vary in the range $[\mathcal{B}, 2\mathcal{B}]$ depending on the relative position. The field measured by the two functional axes of the magnetometer is a 2D vector:

$$\mathbf{b}_m = \mathcal{B}\mathbf{P}\mathbf{R}_x(\phi)^T\mathbf{R}_y(\theta)^T\mathbf{R}_z(\psi)^T \left(\frac{3\mathbf{p}_c\mathbf{p}_c^T}{\|\mathbf{p}_c\|^2} - \mathbf{I} \right) \frac{\mathbf{m}_e}{\|\mathbf{m}_e\|} \quad (5)$$

where \mathbf{P} is a matrix that extracts the components of field corresponding to the sensing directions. If the sensing axes are the x - and y -axes as in Fig. 1(a), then

$$\mathbf{P} = \begin{bmatrix} 1 & 0 & 0 \\ 0 & 1 & 0 \end{bmatrix}.$$

If they are the y - and z -axes as in Fig. 1(b), then

$$\mathbf{P} = \begin{bmatrix} 0 & 1 & 0 \\ 0 & 0 & 1 \end{bmatrix}.$$

To estimate the capsule's position and the angle ψ we take n magnetometer measurements, $\mathbf{b}_{m,i}$, corresponding to n distinct known external dipole moments, $\mathbf{m}_{e,i}$, applied when each measurement was taken. Rather than continuously rotating the external dipole as in [12], we have chosen to rotate the external dipole about the cardinal axes of the world frame such that the dipole moment can be thought of as tracing out three arcs in the positive octant (Fig. 3), in an attempt to maximize linear independence between the $\mathbf{m}_{e,i}$. We then use the nonlinear least-squares Levenberg-Marquardt algorithm, which has been shown to outperform other optimization methods in similar problems [3], to minimize the cost function $c = \|\mathbb{B}_m - \mathbb{B}_e\|^2$, where \mathbb{B}_m is a $2n \times 1$ array of magnetometer measurements, and

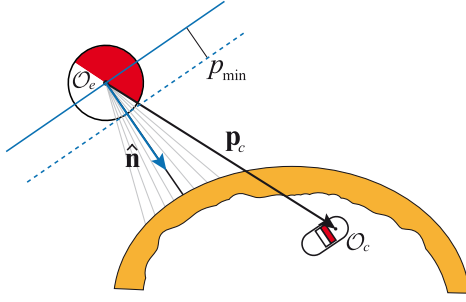


Fig. 4. The dividing plane intersects O_e . The unit normal of this plane, \hat{n} , points to the nearest point on the patient's abdomen. It is assumed that $\hat{n}^T \mathbf{p}_c > p_{\min}$.

\mathbb{B}_e is a $2n \times 1$ array containing corresponding expected magnetometer measurements using (5) for each $\mathbf{m}_{e,i}$ at the current best estimate of the pose. The Levenberg-Marquardt algorithm iteratively updates the pose until a local minimum of c is found. We allow \mathbf{p}_c and ψ to be updated at each iteration, keeping θ and ϕ fixed. We use a numerically approximated Jacobian for the optimization, both in MATLAB with the *lsqnonlin()* function and in C++ with the NonLinearOptimization module of the Eigen library [19]. In our implementation, we take advantage of the fact that we must take n magnetometer measurements by simultaneously collecting n accelerometer measurements, which are averaged to produce \mathbf{g} used by (2) and (3) to compute θ and ϕ .

The method above assumes that magnetometer biases due to the internal magnet and the Earth's magnetic field have been removed. This is accomplished by averaging a batch of low-applied-field magnetometer data to measure, and then remove, the bias. If the dipole field source is an electromagnet, the field should simply be turned off during this data collection. If the dipole field source is a permanent magnet, it should be moved far away from possible positions of the capsule, and the data collection should be divided into two halves, wherein the otherwise-arbitrary direction of \mathbf{m}_e used in one half is opposite (i.e., rotated by 180°) from that used in the other half.

From exhaustive simulations in a pilot study, and assuming that we have a sufficiently rich data set, we find there are two global minima to the cost function c . One corresponds to the true pose $\{\mathbf{p}_c, \mathbf{R}_c\}$ and the other is a pose at the mirrored position $-\mathbf{p}_c$ with the same orientation. In order to differentiate the true pose from the mirrored pose, it is necessary to define a plane such that the true pose and the mirrored pose will fall on opposite sides. We use our knowledge that the capsule will reside inside the patient's abdomen to define this dividing plane as shown in Fig. 4. We define the plane such that it intersects the center of the external magnetic dipole. The normal of the plane, \hat{n} , is defined as the unit-normalized vector from the center of the external dipole to the nearest point on the surface of the patient's abdomen (e.g., determined via RGB-D camera). If the position \mathbf{p}_c resulting from the Levenberg-Marquardt optimization is correct, then $\hat{n}^T \mathbf{p}_c > 0$. Otherwise, \mathbf{p}_c must be negated. The presence of noise can cause the above method to fail when \mathbf{p}_c is very near the plane. This is because the optimization may converge to a position that

is close to the true position but on the wrong side of the plane. To prevent this, it is important that $\hat{n}^T \mathbf{p}_c > p_{\min}$, where $p_{\min} > 0$ is the minimum distance of the true position from the dividing plane. For any real magnetic field source, this distance can be determined and enforced.

COTS magnetometers vary widely in range (typically ± 0.2 – 150 mT) and resolution Δ (typically 0.001 – 73 μ T per least significant bit), and there exists a trade-off between these two parameters. Furthermore, the details of a particular capsule design and locomotion scheme play a non-trivial role in the external dipole magnitude (or distance from the capsule) required to maintain the assumption that the capsule is stationary during localization. To generalize our results such that they can be applied across a variety of magnetic capsule endoscopes, we introduce a nondimensional nominal field strength, \mathcal{B}/Δ , which represents the number of magnetometer quantization steps used to resolve the nominal field experienced by the capsule during localization; it captures the relative contributions of the dipole strength, the distance between the dipole and the capsule, and the magnetometer resolution.

III. SIMULATIONS

Simulations were conducted in MATLAB to establish expected performance. In all simulations, the workspace was taken to be the lower hemisphere (i.e., in the $-\mathbf{z}_w$ direction, with O_e and O_w coincident) of a sphere with radius 400 mm centered at the center of the external dipole. Random test poses were uniformly sampled from this workspace such that $\|\mathbf{p}_c\| > 20$ mm and $-\mathbf{z}_w^T \mathbf{p}_c > 25.4$ mm. In addition to these random poses, three special-case poses were tested, which we (incorrectly) hypothesized had a higher likelihood of exhibiting some sort of singularity in the method: all three poses are positioned directly below the external dipole (at $\|\mathbf{p}_c\| = 200$ mm, without loss of generality), with orientations such that the magnetic sensing plane is orthogonal to each of the cardinal axes of the world frame. We chose the dipole strength to be the same as that used in our experimental hardware (discussed in the following section). Assuming the sensor resolution from our experiments, the range of \mathcal{B}/Δ is $[6.9 \times 10^1, 5.5 \times 10^5]$ for these simulations (note that this range is slightly larger than the steps available with a 20-bit analog-to-digital converter (ADC)).

Initial simulations were performed with $1,000,000$ random test poses, and without modeling noise or uncertainty of any kind. Under these conditions, we investigated the set of dipole moments, $\mathbf{m}_{e,i}$, necessary to localize successfully. We found that a set of three orthogonal moments aligned with the positive cardinal axes of the world frame are sufficient (i.e., the solid red vectors in Fig. 3). Using these applied moments, the algorithm estimates the capsule pose with negligible error (dependent largely on optimization stopping criteria) in position (2.6×10^{-9} mm) and orientation (1.2×10^{-7} deg), where we compute orientation error using the angle-axis representation. However, only 99.83% of the test poses succeed. As Levenberg-Marquardt optimization is an iterative procedure, the choice of initial condition may result in a local minimum that results in a localization failure. To combat this, it is common practice

TABLE I
SIX INITIAL CONDITIONS THAT PRODUCE 100% SUCCESS RATE WHEN USED TOGETHER. $\|\mathbf{p}_c\| = 140$ mm IN ALL CASES

Initial Position \mathbf{p}_c [mm]	Initial Angle ψ [deg]
$[-81 \ -81 \ -81]^T$	0
$[110 \ -30 \ -81]^T$	0
$[-30 \ 110 \ -81]^T$	0
$[-81 \ -81 \ -81]^T$	180
$[110 \ -30 \ -81]^T$	180
$[-30 \ 110 \ -81]^T$	180

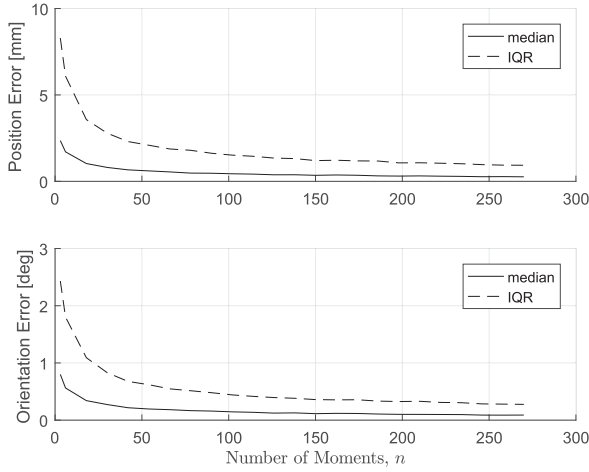


Fig. 5. Median and interquartile range of position and orientation error as a function of the number of applied moments used when collecting magnetometer measurements. Error at each number of moments was computed over 10,000 random test poses.

to optimize multiple times using several initial conditions and keep the best result; this increases the likelihood that at least one initial condition might arrive at the global minimum. We found that a set of six initial conditions spaced evenly throughout our workspace is sufficient to achieve 100% success in simulation over 1,000,000 random test poses. Those six initial conditions are provided in Table I.

To investigate the effect of sensor noise on localization, zero-mean Gaussian sensor noise was added to the model, based on our experimental hardware. As the noise characteristics of our magnetometer and accelerometer are not the same for all three axes, we use the worst-case values from each sensor, which have standard deviations of $10.6 \mu\text{T}$ and 0.002 G , respectively. Including this noise results in median errors of 2.4 mm and 0.8° with interquartile ranges (IQR) of 8.3 mm and 2.4° over 10,000 random poses. This error is reduced by using additional distinct applied moments, $\mathbf{m}_{e,i}$. We add moments such that they are spaced evenly along the arcs of the octant formed by the cardinal axes (i.e., $n/3$ moments reside on each arc, see Fig. 3). Fig. 5 shows the error statistics as a function of the number of distinct applied moments. Increasing the number of moments reduces error, but it also increases the data collection time, which

can be computed as $n(t_r + t_m + t_w)$ where t_r is the time for the external dipole to rotate between moment orientations, t_m is the sensor measurement time, and t_w is the wireless data transmission time. We chose to use $n = 135$ moments in the following, which corresponds to an angular spacing of 2° along each arc, as a balance between accuracy and data collection time.

IV. EXPERIMENTS

In our experiments, we used a spherical-actuator-magnet manipulator (SAMM) as the external dipole-field source [20]; our SAMM contains a spherical Grade-N42 NdFeB permanent magnet, which is assumed to be uniformly magnetized (and thus having a field that is perfectly modeled by (4) [21]), with radius 25.4 mm and dipole strength $\|\mathbf{m}_e\| = 66.0 \text{ A} \cdot \text{m}^2$. The SAMM is mounted as the end-effector of a Yaskawa Motoman 6-DOF robotic arm (see Fig. 2), serving as a spherical wrist.

We chose to use a Melexis MLX90393 3-axis magnetometer and a TDK ICM-42605 6-axis IMU as the “internal” sensors. Both sensors are surface-mounted integrated circuits, each measuring approximately $3 \times 3 \times 1$ mm. Each axis of the magnetometer uses a 16-bit ADC with a sensing range of up to ± 50 mT and can optionally be turned off to reduce power consumption. The IMU contains a 3-axis accelerometer; each axis was configured to measure $\pm 2 \text{ G}$ using a 16-bit ADC.

An nRF52832 System-on-Chip (SoC) from Nordic Semiconductor was used to communicate with the sensors over an I²C bus running at 400 kbps and relay the measurements wirelessly to the host computer using Bluetooth Low Energy. This SoC comes in 6×6 mm and 3×3.2 mm surface-mount package variants and requires a 2.4 GHz antenna to communicate over Bluetooth. Measurements from both sensors were taken every 10 ms and transmitted to the host computer in groups of five every 50 ms.

We constructed a sensing stage using breakout and evaluation boards for the selected sensors and SoC, which functionally matches what one would construct for an actual capsule (Fig. 6). The magnetometer breakout board and the IMU evaluation board are rigidly attached to a 3D-printed stage using nylon fasteners. Note that the exact IMU placement is not relevant since a measurement of the direction of gravity can be done from any position on the stage. The relative orientation of the magnetometer and IMU is fixed, which is important. The IMU evaluation board has been modified to make it function as a simple breakout board; none of the other components on this board are used in our experiments. The stage has three sets of holes that orient the sensors’ xy -plane horizontally, vertically, or at a 45° angle when mounted in the SAMM workspace (Fig. 6(c)). Nylon fasteners are also used to mount the stage itself. The SAMM can be positioned arbitrarily by the robotic arm (Fig. 6(a)). Thus, our setup is capable of testing for arbitrary positions \mathbf{p}_c , at three different orientations.

A small magnet is positioned directly adjacent to the magnetometer, as it would be in a typical capsule design (Fig. 6(d)). We can interchange a NdFeB Grade-N50 disc magnet with a diameter of 10 mm and thickness of 3 mm that is either axially

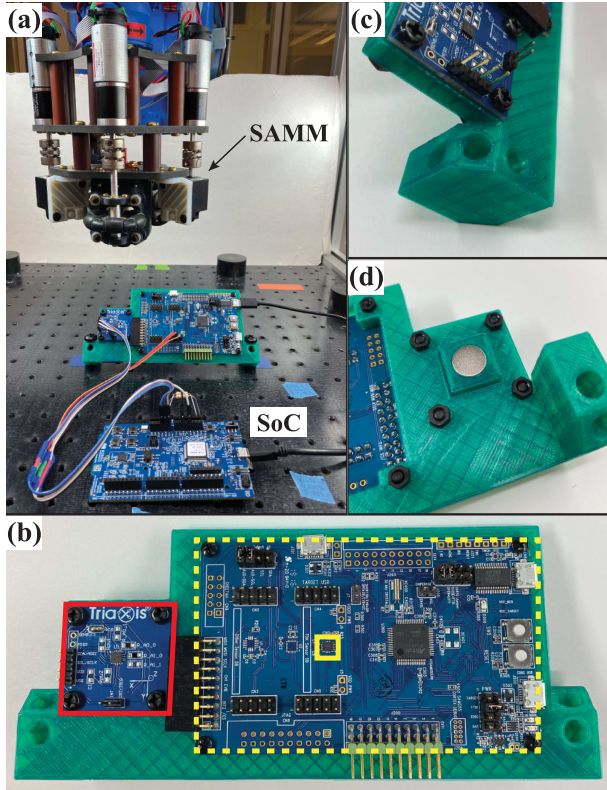


Fig. 6. The experimental hardware and setup. (a) The SAMM shown near the sensor stage, which is mounted in the 45° orientation and connected via I²C to the nRF52832 SoC development board. The two black USB cables are used for power only; all communication with the “internal” electronics is performed wirelessly. (b) The sensor stage containing the magnetometer (solid red box) and the IMU (solid yellow box) on the evaluation board (dotted yellow box). (c) Mounting holes for horizontal, 45° , or vertical orientation. (d) An interchangeable disc magnet is positioned adjacent to the magnetometer.

or diametrically magnetized (as in Fig. 1). When using the axially magnetized magnet, both magnetometer sensing axes have the same resolution of $\Delta = 1.502 \mu\text{T}$ per least significant bit. When using the diametrically magnetized magnet, one magnetic sensing axis (z_c) has a reduced resolution of $\Delta = 2.420 \mu\text{T}$ per least significant bit.

Experiments were conducted to validate the localization method using the hardware described above. In each experiment, the external magnetic dipole (SAMM) was placed at 216 positions arranged in a box grid centered above the magnetometer frame (\mathcal{O}_c). The grid measures 250×250 mm horizontally and has a vertical height of 100 mm. It consists of six evenly spaced horizontal-plane layers, each with $6 \times 6 = 36$ evenly spaced points, which results in a horizontal spacing of 50 mm and a vertical spacing of 20 mm. The bottom of the grid is placed 85 mm above the center of the magnetometer. At each position, localization was performed and the resulting pose estimate was compared to the true pose, which is known with sub-millimeter accuracy. The grid was repeated for all possible combinations of sensing stage orientation and internal-magnet magnetization direction. For these experiments, $t_m + t_w = 50$ ms (because the measurements were transmitted in batches) and $t_r \approx 180$ ms. Computation time for the localization algorithm can vary (we

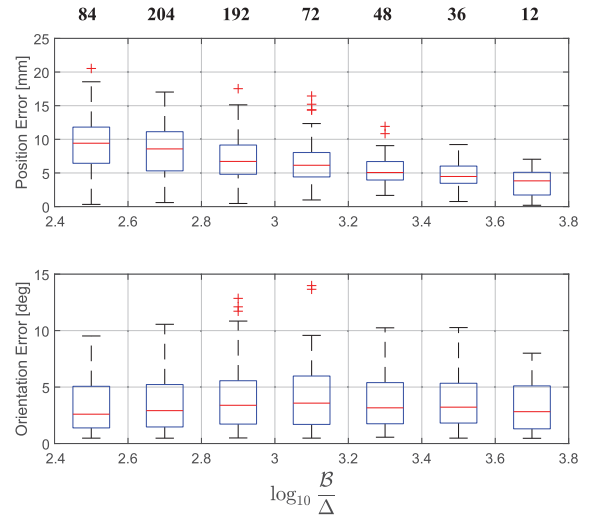


Fig. 7. Box-whisker plot of localization error for the axially magnetized magnet as a function of $\log_{10} (B/\Delta)$. The number of samples in each 0.2-width region of $\log_{10} (B/\Delta)$ is provided in bold at the top of the figure.

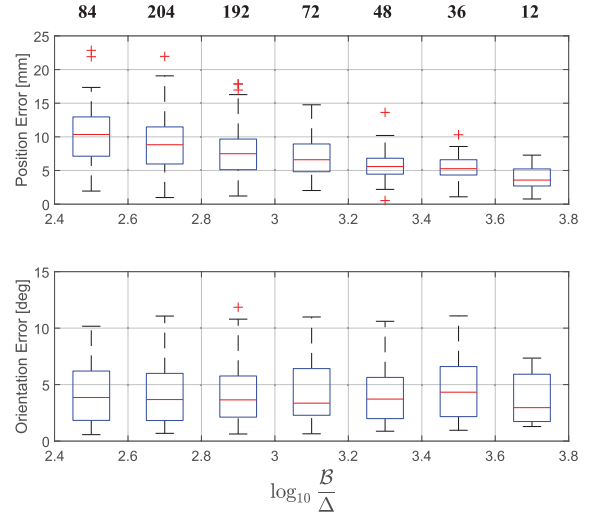


Fig. 8. Box-whisker plot of localization error for the diametrically magnetized magnet as a function of $\log_{10} (B/\Delta)$. The number of samples in each 0.2-width region of $\log_{10} (B/\Delta)$ is provided in bold at the top of the figure.

observed 7 ms on average). Figures 7 and 8 show the distribution of position and orientation error—for the axially and diametrically magnetized magnets, respectively—as a function of $\log_{10} (B/\Delta)$. The box-whisker plots include all of the data from the three orientations, such that orientation serves as a source of variance in the localization error. In the case of the diametrically magnetized magnet, in our nondimensionalization we use the conservative value of Δ provided above.

V. DISCUSSION

With the proposed method, error decreases as B/Δ increases. This trend is expected because larger B/Δ approaches an ideal continuous sensor. Indeed, B/Δ was varied in our experiments by changing $\|\mathbf{p}_c\|$ and since the field strength from the external dipole decreases cubically with distance, this results in poorer

signal-to-noise ratios at greater distances. This is in spite of the fact that the point-dipole model (4) becomes increasingly accurate with distance from any field source [18]. Orientation errors were fairly insensitive to \mathcal{B}/Δ , and were largely within what would be considered “small angles” across the values considered. This is likely due to the heavy reliance on the accelerometer to form the estimate of orientation. Position errors increase substantially with small \mathcal{B}/Δ . Although our localization method may not outperform the best of other magnetic-field-based methods, its advantages in terms of reduced complexity, size, and power consumption (it does not require sensors to completely surround the internal magnet as in [10]–[13]) make it a useful alternative, given realistic capsule design constraints.

We were interested in why the localization errors were larger in our experimental results than in our simulations (which included realistic sensor noise). We investigated probable sources of error. The temperature-dependent gain used to convert 16-bit raw magnetometer readings to units T was taken directly from the data sheet. Using previously recorded data, we found that tuning this gain produced no more than a 0.5 mm reduction in mean position error and negligible reduction in orientation error. We also considered the possibility that the workspace to which the sensor stage is mounted was not level, thus producing incorrect estimates of the direction of gravity. We found that our workspace was out of level by 0.5° . Correcting for this produced a reduction in position error of 0.2 mm and a reduction in orientation error of approximately 0.5° . There may also be some small error in the estimate of the orientation of the SAMM’s magnet, although its control system was set with a convergence criterion of 1° , or distortions in its field not captured by the point-dipole model, although the point-dipole model is known to be very accurate for spherical magnets.

Our method assumes the capsule is stationary during localization. To explore this assumption for our specific permanent-magnet system used in this work (SAMM [20]), which we have used in many other previous works, we consider the case in which the external magnet is placed directly above a 4 g screw-type dummy capsule measuring 26 mm in length and 14 mm in diameter and containing a 6.35-mm cubic Grade-N52 NdFeB permanent magnet that was placed inside *ex vivo* porcine intestines. At distances of more than 217 mm, the capsule rotated less than 5° . At distances of more than 265 mm, the capsule produces a nearly imperceptible trembling. At distances of more than 316 mm, the capsule does not move at all to the naked eye. At this final “no movement” distance, the largest field from the SAMM experienced by the magnetometer is $\pm 420 \mu\text{T}$. Using a COTS Memsic MMC5633NJL magnetometer, which has a resolution of 6.25 nT per least significant bit and a range of $\pm 3 \text{ mT}$, we would achieve $\log_{10}(\mathcal{B}/\Delta) = 4.5$, which is at least as accurate as our most accurate experiments.

In [11], we demonstrated that the sensor arrangement of [12] enabled simultaneous localization and propulsion of a screw-type capsule, using the method of [12] to perform the initial localization. It is left as an open question if the sensor arrangement described in this letter will enable such capabilities. However, it would certainly require a magnetometer that can handle the relatively high field strengths experienced during

magnetic propulsion. This seems to suggest that a capsule that contains two 2-axis magnetometers—one with a large range but poor resolution, and one with a small range and fine resolution—may be a desirable arrangement for a complete localization system. Such an arrangement would still be simpler and more compact than the arrangement in [12].

REFERENCES

- [1] N. Shamsudhin *et al.*, “Magnetically guided capsule endoscopy,” *Med. Phys.*, vol. 44, no. 8, pp. e91–e111, 2017.
- [2] F. Bianchi *et al.*, “Localization strategies for robotic endoscopic capsules: A review,” *Expert Rev. Med. Devices*, vol. 16, no. 5, pp. 381–403, 2019.
- [3] C. Hu, M. Q.-H. Meng, and M. Mandal, “Efficient linear algorithm for magnetic localization and orientation in capsule endoscopy,” in *Proc. IEEE Eng. Med. Biol. Soc. Conf.*, 2005, pp. 7143–7146.
- [4] C. Hu *et al.*, “A cubic 3-axis magnetic sensor array for wirelessly tracking magnet position and orientation,” *IEEE Sens. J.*, vol. 10, no. 5, pp. 903–913, May 2010.
- [5] D. Son, S. Yim, and M. Sitti, “A 5-D localization method for a magnetically manipulated untethered robot using a 2-D array of Hall-effect sensors,” *IEEE/ASME Trans. Mechatronics*, vol. 21, no. 2, pp. 708–716, Apr. 2016.
- [6] S. Song, C. Hu, and M. Q.-H. Meng, “Multiple objects positioning and identification method based on magnetic localization system,” *IEEE Trans. Magn.*, vol. 52, no. 10, pp. 1–4, Oct. 2016, Art. no. 9600204.
- [7] S. Song, X. Qiu, W. Liu, and M. Q.-H. Meng, “An improved 6-D pose detection method based on opposing-magnet pair system and constraint multiple magnets tracking algorithm,” *IEEE Sens. J.*, vol. 17, no. 20, pp. 6752–6759, Oct. 2017.
- [8] Y. Xu and M. Q.-H. Meng, “Free sensor array based relative localization system for wireless capsule endoscopy,” in *Proc. IEEE Int. Conf. Robot. Biomimetics*, 2018, pp. 550–555.
- [9] D. Son, X. Dong, and M. Sitti, “A simultaneous calibration method for magnetic robot localization and actuation systems,” *IEEE Trans. Robot.*, vol. 35, no. 2, pp. 343–352, Apr. 2019.
- [10] C. Di Natali, M. Beccani, N. Simaan, and P. Valdastri, “Jacobian-based iterative method for magnetic localization in robotic capsule endoscopy,” *IEEE Trans. Robot.*, vol. 32, no. 2, pp. 327–338, Apr. 2016.
- [11] K. M. Popek, T. Hermans, and J. J. Abbott, “First demonstration of simultaneous localization and propulsion of a magnetic capsule in a lumen using a single rotating magnet,” in *Proc. IEEE Int. Conf. Robot. Automat.*, 2017, pp. 1154–1160.
- [12] K. M. Popek, T. Schmid, and J. J. Abbott, “Six-degree-of-freedom localization of an untethered magnetic capsule using a single rotating magnetic dipole,” *IEEE Robot. Autom. Lett.*, vol. 2, no. 1, pp. 305–312, Jan. 2017.
- [13] A. Z. Taddese, P. R. Slawinski, M. Pirotta, E. De Momi, K. L. Obstein, and P. Valdastri, “Enhanced real-time pose estimation for closed-loop robotic manipulation of magnetically actuated capsule endoscopes,” *Int. J. Robot. Res.*, vol. 37, no. 8, pp. 890–911, 2018.
- [14] A. W. Mahoney and J. J. Abbott, “Five-degree-of-freedom manipulation of an untethered magnetic device in fluid using a single permanent magnet with application in stomach capsule endoscopy,” *Int. J. Robot. Res.*, vol. 35, no. 1–3, pp. 129–147, 2016.
- [15] H. Zhou, G. Alici, T. D. Than, and W. Li, “Modeling and experimental characterization of propulsion of a spiral-type microrobot for medical use in gastrointestinal tract,” *IEEE Trans. Biomed. Eng.*, vol. 60, no. 6, pp. 1751–1759, Jun. 2013.
- [16] Y. Xu, K. Li, Z. Zhao, and M. Q. Meng, “Improved multiple objects tracking based autonomous simultaneous magnetic actuation & localization for WCE,” in *Proc. IEEE Int. Conf. Robot. Automat.*, 2020, pp. 5523–5529.
- [17] A. J. Petruska and J. J. Abbott, “Omnimagnet: An omnidirectional electromagnet for controlled dipole-field generation,” *IEEE Trans. Magn.*, vol. 50, no. 7, pp. 1–10, Jul. 2014, Art. no. 8400810.
- [18] J. J. Abbott, E. Diller, and A. J. Petruska, “Magnetic methods in robotics,” *Annu. Rev. Control Robot. Auton. Syst.*, vol. 3, pp. 57–90, 2020.
- [19] G. Guennebaud *et al.*, “Eigen v3,” 2010. [Online]. Available: <http://eigen.tuxfamily.org>
- [20] S. E. Wright, A. W. Mahoney, K. M. Popek, and J. J. Abbott, “The spherical-actuator-magnet manipulator: A permanent-magnet robotic end-effector,” *IEEE Trans. Robot.*, vol. 33, no. 5, pp. 1013–1024, Oct. 2017.
- [21] E. P. Furlani, *Permanent Magnet and Electromechanical Devices: Materials, Analysis, and Applications*. San Diego, CA, USA: Academic Press, 2001.